Available online at www.sciencedirect.com

Manufacturing Letters

Manufacturing Letters 41 (2024) 1440–1451

52nd SME North American Manufacturing Research Conference (NAMRC 52, 2024)

Machine Tool Thermal Error Measurement and Prediction via Wireless Microscope

Zongze Li[a], Gregory W. Vogl[b], Edward C. Kinzel[a], Botond Santa[a], Robert G. Landers[a,*]

[a] *University of Notre Dame, Notre Dame, Indiana 46556, USA*
[b]*National Institute of Standards and Technology, 100 Bureau Drive, Gaithersburg, Maryland 20899-8220, USA*

* Corresponding author. *E-mail address:* rlanders@nd.edu

Abstract

A novel method is proposed to measure the thermal errors of a three-axis machine tool by taking images of unique custom-designed fiducials attached to a worktable using a wireless microscope mounted to the spindle. Multiple fiducials are applied for the measurement of different thermal errors at various worktable locations. In addition, a least-squares thermal error model within the work volume is proposed in which the model parameters are determined from various fiducial measurements, and the use of various fiducials for the thermal error model is analyzed. The results show the method can measure thermal errors within four times the positioning resolution of the machine tool, with most of the errors being smaller in magnitude than twice the positioning resolution. Further, the results show the thermal error model depends on the location of the fiducials used to construct the model. The unique numbering system for the fiducial patterns also allows for the measurement of large planar thermal errors, which is advantageous for machine tools that undergo significant thermal drift.

© 2024 The Authors. Published by ELSEVIER Ltd. This is an open access article under the CC BY-NC-ND license (https://creativecommons.org/licenses/by-nc-nd/4.0)
Peer-review under responsibility of the scientific committee of the NAMRI/SME.
Keywords: Machine tool thermal error

1. Introduction

Machine tool error sources are generally classified as four types: geometric errors, servo dynamics, thermal errors, and deformations/vibrations due to cutting forces [1, 2]. Thermal errors affect machining accuracy through the thermal deformations of the machine tool structural components due to temperature variations from internal heat sources (e.g., motors) and environment temperature changes. Thermal errors can contribute up to 75 percent of the overall machining errors of a machined part [3]. Especially for large-volume parts, the machining errors can be mainly attributed to thermal error effects [4, 5].

In general, there are two methods for thermal error reduction: thermal error avoidance and thermal error compensation. Thermal error avoidance techniques make the machine tool less sensitive to temperature variations. These techniques include the use of materials with reduced friction and low coefficients of thermal expansion, optimization of lubrication and cooling systems, etc. [6, 7]. In contrast, thermal error compensation is normally based on a predictive model established by the thermal error measurement of a machine tool. Thermal error avoidance is typically a more costly solution than thermal error compensation and is more sensitive to modeling errors and unknown disturbances [8].

Thermal error compensation strategies typically employ a predictive error model, which are inverted to determine compensation amounts. Common thermal error models include least-square regression, finite element, neural network, gray system, etc. These models predict machine tool thermal deformation from the structure geometry, material, ambient temperature, and heat generation from various sources [9-10]. In terms of thermal error compensation strategies, Cui et al. [11] designed a novel error compensator, hooking up with Simens 840D CNC systems, and experimental results shows

2213-8463 © 2024 The Authors. Published by ELSEVIER Ltd. This is an open access article under the CC BY-NC-ND license (https://creativecommons.org/licenses/by-nc-nd/4.0)
Peer-review under responsibility of the scientific committee of the NAMRI/SME.

that the errors along three axes were reduced by more than 50%. Gebhardt et al [12] developed a thermal error compensation method based on a grey box to reduce the effect caused by machine tool internal heat source, and 85% of the thermal errors were compensated experimentally. Zimmermann et al [13] presented a for thermal error compensation strategy where a Thermal Adaptive Learning Control methodology is adopted to define the optimal inputs for the error compensation, and through testing on a 5-axis machine tool, the compensation robustness was significantly increased.

Thermal error measurement methods for compensation are classified as indirect and direct. Indirect measurement methods estimate the thermal deformation of a machine tool based on a temperature-deformation simulation model (e.g., finite element, neural network) and measure temperatures via thermocouples or thermal cameras [14, 15]. However, this method usually requires the use of complex metrology equipment and high-fidelity simulation models that are computationally intensive. Alternatively, direct measurement methods measure the changes of the tool position relative to the workpiece via displacement sensors such as laser interferometers, capacitive sensors, and touch probes [16-18].

For direct measurements, multi-position measurements are necessary to determine the thermal errors effects on the entire machine tool workspace [19], which is usually a very time-consuming measurement process. Therefore, alternative approaches have been proposed. To conduct a quick measurement of thermal errors, Ibaraki and Mori et al. [20, 21] proposed a two-dimensional trajectory for tracking an interferometer measurement to evaluate the thermal errors of a five-axis machine tool. Brecher et al. [22] proposed a thermal error measurement system via a position sensing detector and a thermally-stable laser frame, through which changes of the 13 kinematic errors of a three-axis machine tool were obtained.

In this study, a novel measurement method is proposed for direct thermal error measurement. The measurement method can be rapid, accurate, inexpensive, and practical for industrial usage. The measurement is implemented by taking images of custom-designed fiducials attached to the worktable from a wireless microscope mounted into the spindle, and the three-dimensional displacement at each fiducial is calculated through image analysis.

The content of this paper is as follows: The measurement equipment is described in Section 2 and the measurement method and image-processing method to obtain three-dimensional displacements are introduced in Section 3. In Section 4, a linear thermal error model is proposed, a thermal error prediction method is described, and experimental results are provided and discussed. The paper is then summarized, and conclusions are drawn in Section 5.

2. Measurement method

2.1. Wireless microscope

A wireless digital microscope (MX200-B, TTAKMLY LLC†) is applied for thermal error measurement, as shown in Fig. 1a. The digital microscope has a complementary metal-oxide-semiconductor (CMOS) sensor, a pixel range of 1920×1080, and a 10 MB bandwidth Wi-Fi function. Images and recorded videos can be saved on mobile devices such as smart phones, tablets, etc. The microscope is mounted to the spindle through a microscope holder, as shown in Fig. 1b. When taking images, machine tool vibration can cause errors; therefore, all images are taken after machine tool vibration ceases.

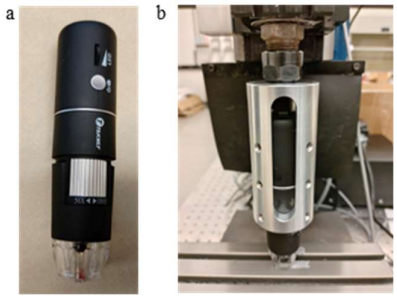

Fig. 1: (a) Microscope utilized in experimental studies and (b) microscope holder.

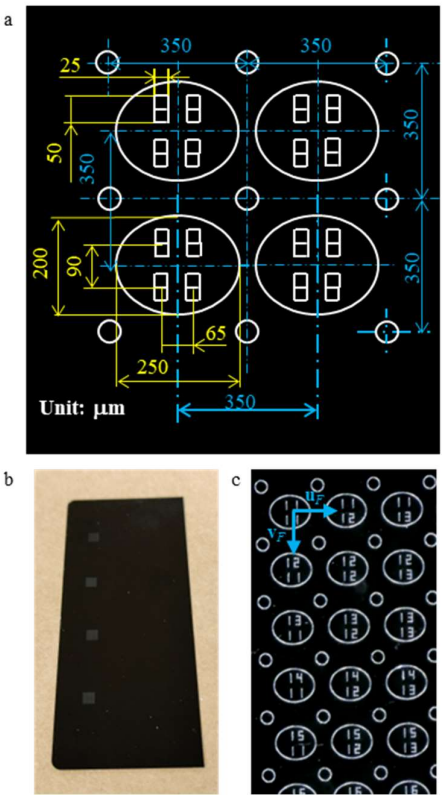

Fig. 2: (a) Fiducial subset schematic with dimensions, (b) photograph of four fiducials, and (c) fiducial microscope image with fiducial coordinate frame.

2.2. Fiducial

In this study, fiducials with a novel pattern-map as shown in Fig. 2a are used. The fiducials consist of a grid of uniformly spaced circles and a grid of uniformly spaced ellipses. The ellipses contain four unique digits arranged in a 2×2 pattern. The two digits of the first row, starting from 11, indicate the ellipse row number, and the two digits of the second row,

starting from 11 as well, indicate the ellipse column number. The grid of circles is used to calibrate the pixel length, and the grid of ellipses is used to determine displacements. The ellipses are on a 9×9 grid for the fiducials used in this study, thus, each fiducial contains 81 ellipses. The schematic in Fig. 2a is a subset of the entire fiducial. Both the distances between circles and the distances between ellipses are 350 μm. The pattern-map is fabricated on black aluminum sheets by a femtosecond laser (Pharos PH1-20, Light Conversion Inc.) on a motion stage with a resolution of 75 nm. Four fabricated fiducials are shown in Fig. 2b, and the microscope view of a fiducial is shown in Fig. 2c.

To determine machine tool displacements in the XY plane, a fiducial coordinate frame, denoted FCF, is defined whose origin is located at the centroid of the subset pattern with the index 11 in both rows, as shown in Fig. 2c. The FCF X-axis, given by unit vector $\mathbf{u}_F$, is along the column index increasing direction, and the FCF Y-axis, given by unit vector $\mathbf{v}_F$, is along the row index increasing direction, as shown in Fig. 2c. The nominal centroid coordinate (in μm) of each subset pattern in the FCF is

$$\begin{aligned}\left[x_{m,n}\right]_F &= (n-11)\cdot 350 \\ \left[y_{m,n}\right]_F &= (m-11)\cdot 350\end{aligned} \tag{1}$$

where $[x_{m,n}, y_{m,n}]_F$ is the nominal centroid of the ellipse in the m^{th} row and n^{th} column.

The subset pattern location identification method consists of calculating the correlation coefficient between the identified numbers and images of numbers stored in the Number Library, as shown in Fig. 3. The images are transformed into binary images, and the binarization threshold value is tailored for each fiducial (0.2-0.3 for the eight fiducials used in this study). The centroid coordinate in the image coordinate frame, denoted ICF, and pattern tilt angle, denoted θ in Fig. 4a, of each ellipse are identified using the function 'regionprop' in the MATLAB Image Processing Toolbox. Then, each ellipse image is rotated by the pattern tilt angle as shown in Fig. 4b. To remove the ellipse edge and isolate the numbers, the subset pattern is divided into four parts by the ellipse major and minor axes lines of the ellipse and the remaining ellipse arcs are removed, as shown in Fig., 4c. To calculate the correlation coefficient between the identified numbers and the numbers in the Number Library, the identified number images are resized to the same dimension as the number images in the Number Library, and the correlation coefficient between each microscope number image and each standard number image in the Number Library is calculated as

$$rc_{i,j} = \frac{\sum_{p=1}^{m}\sum_{q=1}^{n}\left(\mathbf{A}_i(p,q)-\bar{\mathbf{A}}_i\right)\left(\mathbf{B}_j(p,q)-\bar{\mathbf{B}}_j\right)}{\sqrt{\sum_{p=1}^{m}\sum_{q=1}^{n}\left(\left(\mathbf{A}_i(p,q)-\bar{\mathbf{A}}_i\right)^2\right)\cdot\sum_{p=1}^{m}\sum_{q=1}^{n}\left(\left(\mathbf{B}_j(p,q)-\bar{\mathbf{B}}_j\right)^2\right)}} \tag{2}$$

where $\mathbf{A}$ and $\mathbf{B}$ are the grayscale color index value matrices (dimension $m\times n$) of the identified images and the library numbers, respectively, where i = 1,2,3,4 denotes the number location within the given ellipse, j = 1,…,9 denotes the standard number in the Number Library, and $\bar{\mathbf{A}}_i$ and $\bar{\mathbf{B}}_j$, respectively, are

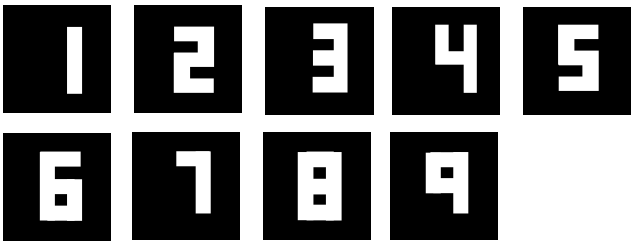

Fig. 3: Number images in Number Library.

Fig. 4: (a) Microscope image of ellipse with number pattern, (b) rotated ellipse, and (c) isolated number from upper left hand ellipse corner.

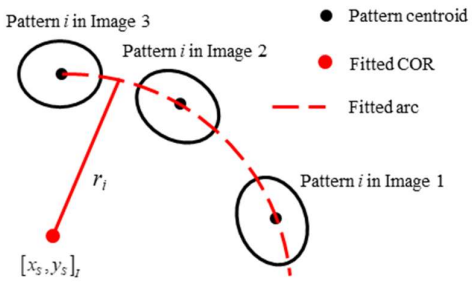

Fig. 5: COR determined using three images from single subset pattern.

$$\bar{\mathbf{A}}_i = \frac{\sum_{p=1}^{m}\sum_{q=1}^{n}\mathbf{A}_i(p,q)}{m\times n} \tag{3}$$

$$\bar{\mathbf{B}}_j = \frac{\sum_{p=1}^{m}\sum_{q=1}^{n}\mathbf{B}_j(p,q)}{m\times n} \tag{4}$$

The identified number for each number location is the number from the Number Library that yields the maximum correlation coefficient, thus determining the subset pattern index.

To avoid image pixel length inaccuracy due to taking images at different microscope heights, the image pixel length, calibrated by the circle grid, is calculated for each image by

$$\Delta d = \frac{350}{\sum_{i=1}^{n}\mathbf{Cd}(i)\Big/n} \tag{5}$$

where $\mathbf{Cd}$ is an $n\times 1$ array consisting of all identified neighboring center-to-center distances of the circle grid.

3. Measurement procedure for one fiducial

3.1. Identification of spindle center of rotation in ICF

To measure errors in the XY plane in the machine tool coordinate frame, denoted MCF, the microscope takes images of a fiducial for each machine tool thermal state (e.g., different ambient temperatures, after the spindle and/or axes have been used for a long period of time) and the thermal errors are determined by computing the displacements of the subset patterns between the images [24]. The subset patterns are rotated about a specific point, the center of rotation COR, which is the projection point of the spindle axis of rotation on the fiducial.

A command position is defined for the microscope where multiple subset patterns of the fiducial can be clearly viewed. At least three images of the multiple subset patterns are taken with different spindle orientations to identify the COR in the ICF. In this study, the authors use three images to identify the COR. The subset pattern centroid coordinates and index numbers are identified for each image. The three centroid coordinates for each unique ellipse pattern are fit to an arc, as shown in Fig. 5. The COR position in the ICF is calculated using the least-squares method

$$\left[[x_S]_I, [y_S]_I, a_1, \cdots, a_n\right]^T = \mathbf{A} \setminus \mathbf{b} \tag{6}$$

$$a_i = [x_S]_I^2 + [y_S]_I^2 - r_i^2 \tag{7}$$

$$\mathbf{A}_{[(2+n)\times(3n)]} = \begin{bmatrix} -2[x_1]_I^{(1)} & -2[y_1]_I^{(1)} & 1 & 0 & \cdots & 0 & 0 \\ -2[x_1]_I^{(2)} & -2[y_1]_I^{(2)} & 1 & 0 & \cdots & 0 & 0 \\ -2[x_1]_I^{(3)} & -2[y_1]_I^{(3)} & 1 & 0 & \cdots & 0 & 0 \\ \vdots & \vdots & \vdots & & \ddots & & \vdots \\ -2[x_n]_I^{(1)} & -2[y_n]_I^{(1)} & 0 & 0 & \cdots & 0 & 1 \\ -2[x_n]_I^{(2)} & -2[y_n]_I^{(2)} & 0 & 0 & \cdots & 0 & 1 \\ -2[x_n]_I^{(3)} & -2[y_n]_I^{(3)} & 0 & 0 & \cdots & 0 & 1 \end{bmatrix} \tag{8}$$

$$\mathbf{b}_{[n\times 1]} = \begin{bmatrix} -[x_1, y_1]_I^{(1)} \square [x_1, y_1]_I^{(1)T} \\ -[x_1, y_1]_I^{(2)} \square [x_1, y_1]_I^{(2)T} \\ -[x_1, y_1]_I^{(3)} \square [x_1, y_1]_I^{(3)T} \\ \vdots \\ -[x_n, y_n]_I^{(1)} \square [x_n, y_n]_I^{(1)T} \\ -[x_n, y_n]_I^{(2)} \square [x_n, y_n]_I^{(2)T} \\ -[x_n, y_n]_I^{(3)} \square [x_n, y_n]_I^{(3)T} \end{bmatrix} \tag{9}$$

where $[x_S, y_S]_I$ is the vector of COR coordinates in the ICF, n is the number of identified subset patterns, r_i is the radius of the i^{th} fitted arc, and $[x_i, y_i]_I^{(j)}$ is the vector of centroid coordinates of the i^{th} subset pattern in the j^{th} image (j = 1, 2, 3).

3.2. MCF calibration

The next part of the procedure is to identify the MCF orientation in FCF. In this study, five images are taken to calibrate the machine tool X- and Y-axis directions in the FCF. A motion path using the five images is obtained and fit to a straight line. Its unit vector indicates the machine tool X- or Y-direction in the ICF, as illustrated in Fig. 6a, where $\mathbf{u}_{IM}$ and $\mathbf{v}_{IM}$ are the unit vectors of the machine tool X- and Y-axes in the ICF, respectively, and $\mathbf{u}_I$ and $\mathbf{v}_I$ are unit vectors of the ICF X- and Y-directions, respectively. Thus, the calibrated vectors $\mathbf{u}_{IM}$ and $\mathbf{v}_{IM}$, respectively, are

$$\begin{aligned} \mathbf{u}_{IM} &= \frac{\sum_{i=1}^{n} \mathbf{u}_{IM,i}}{n} \\ \mathbf{v}_{IM} &= \frac{\sum_{i=1}^{n} \mathbf{v}_{IM,i}}{n} \end{aligned} \tag{10}$$

where n is the number of subset patterns in the image. Figure 7b illustrates the transformation of the machine tool X- and Y-directions from the ICF to the FCF, where $\mathbf{u}_{\text{FM}}$ and $\mathbf{v}_{\text{FM}}$ are the unit vectors of the machine tool X- and Y-axes in the FCF, respectively. From Fig. 6b, the unit vectors of the machine tool X- and Y-axes in the FCF, respectively, are

$$\begin{aligned} \mathbf{u}_{FM} &= \mathbf{u}_{IM} \cdot \left[\mathbf{u}_F{}^T, \mathbf{v}_F{}^T\right] \\ \mathbf{v}_{FM} &= \mathbf{v}_{IM} \cdot \left[\mathbf{u}_F{}^T, \mathbf{v}_F{}^T\right] \end{aligned} \tag{11}$$

3.3. XY displacement

The COR position is the projection of the spindle axis of rotation to a point in the XY plane. Thus, the XY thermal error between two machine tool thermal states is the planar deviation of the COR positions in the MCF. The method to determine the XY tool-to-workpiece displacements between two machine tool thermal states is illustrated in Fig. 7. First, the COR position in the FCF is identified. For one machine tool thermal state as shown in Fig. 7a, the vector from the COR to the centroid of subset pattern i in the FCF is

$$\left[\Delta xc_i, \Delta yc_i\right]_F = \left(\left[x_S, y_S\right]_I - \left[x_i, y_i\right]_I\right) \square \left[\mathbf{u}_F{}^T, \mathbf{v}_F{}^T\right] \tag{12}$$

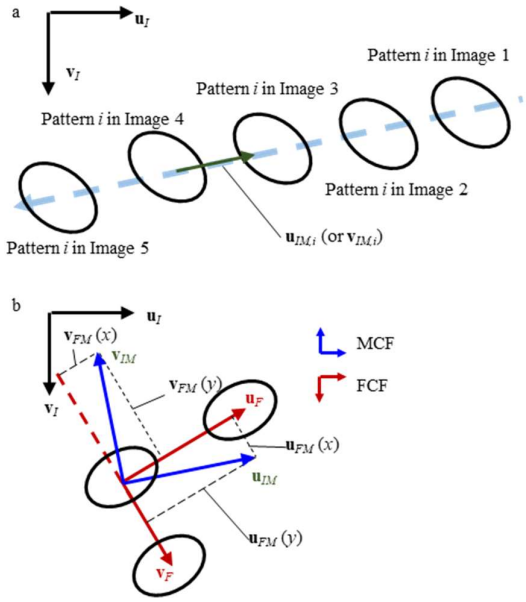

Fig. 6: Machine tool X- and Y-directions in (a) ICF and (b) FCF.

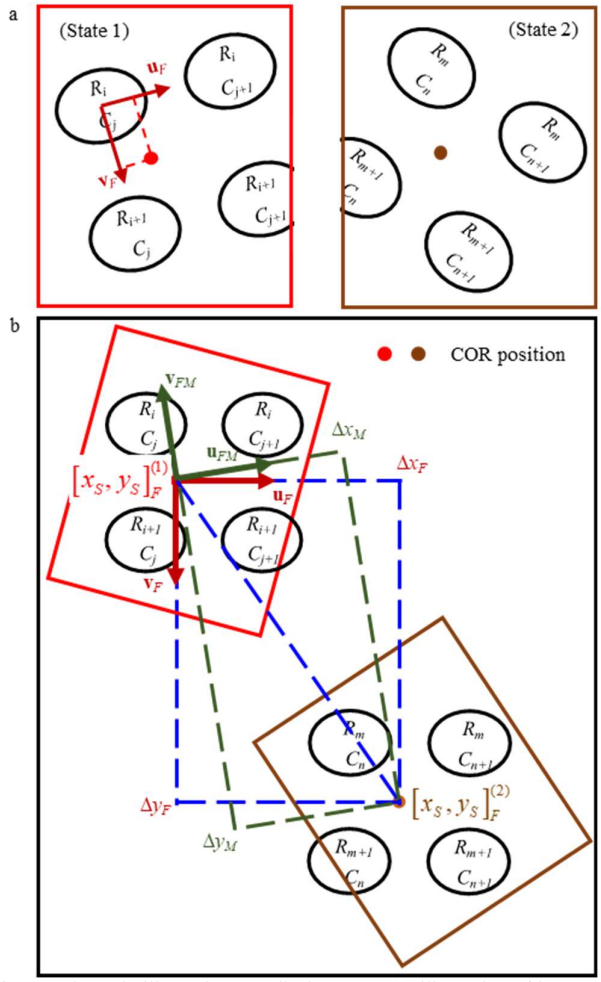

Fig. 7: Schematic illustrating XY displacement. (a) illustration of images of machine tool thermal states 1 and 2, and (b) illustration of two machine tool thermal states in fiducial frame.

where $[\Delta xc_i, \Delta yc_i]_F$ is the vector from the COR to the centroid of the i^{th} subset pattern in the FCF, $[x_i, y_i]_I$ is the centroid coordinates of the i^{th} subset pattern in the ICF, and $\mathbf{u}_F$ and $\mathbf{v}_F$ are unit vectors denoting the FCF X- and Y-directions in the ICF, respectively. The COR position in the FCF is

$$[x_S, y_S]_F = \frac{\sum_{i=1}^{n}\left([\Delta xc_i, \Delta yc_i]_F + [x_i, y_i]_F\right)}{n} \tag{13}$$

where $[x_S, y_S]_F$ is the COR position in the FCF and $[x_i, y_i]_F$ is the centroid coordinates of the i^{th} subset pattern in the FCF, which is defined in Section 2.2. Therefore, the XY machine tool displacements between images 1 and 2 in the FCF and the MCF, respectively, are

$$[\Delta x_F, \Delta y_F] = [x_S, y_S]_F^{(2)} - [x_S, y_S]_F^{(1)} \tag{14}$$

$$[\Delta x_M, \Delta y_M] = [\Delta x_F, \Delta y_F]\cdot[\mathbf{u}_{FM}{}^T, \mathbf{v}_{FM}{}^T] \tag{15}$$

as illustrated in Fig. 7b.

Note that each ellipse within a fiducial is unique because of the unique row-and-column numbering with each ellipse. Therefore, relatively large thermal errors can be tracked that are much greater than the nominal ellipse grid spacing of 350 µm, as shown in Fig. 7b. The row-and-column numbering system for the ellipse pattern allows for the measurement of XY thermal errors that are of any size, whether small or large, compared to the grid spacing. This is clearly advantageous over the use of calibration dots that are nominally identical to each other [24] and useful for large machine tools that may experience large thermal errors.

3.4. Z displacement

A contrast-based method [24] is adopted to compute the machine tool Z-axis displacement. Since the camera focal length is fixed, when the microscope takes images at different Z-axis positions, the contrast of each image will be different. Five images are taken at different machine tool Z-axis command positions and the contrast of each image is calculated by a Gaussian derivative method [23]] with a Gaussian convolution kernel of $2N_w$

$$\Gamma(\hat{x}, \hat{y}) = \frac{1}{2\pi\sigma}\exp\left(-\frac{\hat{x}^2+\hat{y}^2}{2\sigma^2}\right), \begin{cases} -N_w \le \hat{x} \le N_w \\ -N_w \le \hat{y} \le N_w \end{cases} \tag{16}$$

where $\sigma = N_w/2.5$ and the pixel window edge length is $N_w = 7$ [24]. For the j^{th} image ($j = 1,\ldots,5$) of the i^{th} machine tool thermal state the pixel contrast value φ_{ij} at any pixel (x, y) is calculated by the convolution

$$\varphi_{ij}(x,y) = \left[\sum_{\hat{x}=-N_w}^{N_w}\sum_{\hat{y}=-N_w}^{N_w}\Gamma_x(\hat{x},\hat{y})\,g_{ij}(x-\hat{x},y-\hat{y})\right]^2 + \left[\sum_{\hat{x}=-N_w}^{N_w}\sum_{\hat{y}=-N_w}^{N_w}\Gamma_y(\hat{x},\hat{y})\,g_{ij}(x-\hat{x},y-\hat{y})\right]^2 \tag{17}$$

where Γ_x and Γ_y are the partial derivatives of $\Gamma(x, y)$ with respect to x and y, respectively, and $g_{ij}(x, y)$ is the grayscale intensity value at pixel location (x, y). The contrast metric value

ϕ_{ij} for the j^{th} image is

$$\phi_{ij} = \frac{\sum_{x=1}^{N_x}\sum_{y=1}^{N_y}\varphi_{ij}(x,y)}{N_x \times N_y} \tag{18}$$

where N_x and N_y are the dimension of the image in pixels in the x and y directions, respectively.

For the i^{th} machine tool thermal state with five images, the contrast metric vector is $\mathbf{\Phi}_i = [\phi_{i1}, \phi_{i2}, \phi_{i3}, \phi_{i4}, \phi_{i5}]$. In this study, images are taken at -254 µm, -127 µm, 0 µm, 127 µm, and 254 µm from the measurement origin in the machine tool Z-axis direction, and the contrast metric curve is described by a third order spline fit, as shown in Fig. 8.

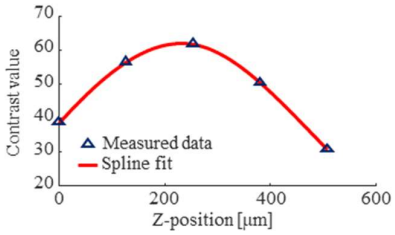

Fig. 8: Contrast metric curve at various Z locations.

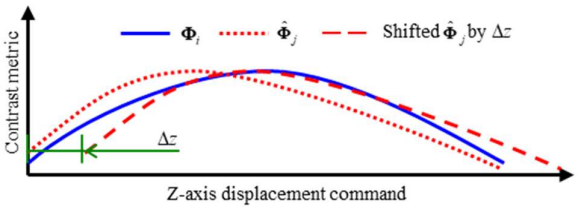

Fig. 9: Original and shifted contrast metric curves.

The Z-axis displacement between two machine tool thermal states is determined by comparing the contrast metric curves for both states. During production, the lighting conditions on the shop floor may vary significantly; therefore, the contrast metric values for the different states are scaled to the same range by

$$\hat{\mathbf{\Phi}}_j = \frac{\max(\mathbf{\Phi}_i)}{\max(\mathbf{\Phi}_j)}\mathbf{\Phi}_j \tag{19}$$

The two contrast metric curves $\mathbf{\Phi}_i$ and $\hat{\mathbf{\Phi}}_j$ are typically very similar as they represent the same Z-axis measurement process; therefore, the Z-axis displacement is identified by determining the displacement shift of $\hat{\mathbf{\Phi}}_j$ that can best align with $\mathbf{\Phi}_i$, as shown in Fig. 9 . To determine the best alignment state for each shift state Δz, the root mean square **RMS**(Δz) is calculated, and the identified Z-axis displacement Δz_M is the shift value Δz where **RMS**(Δz) is minimum, that is

$$\Delta z_M = \underset{\Delta z}{\arg\min}\left(\mathbf{RMS}(\Delta z)\right) \tag{20}$$

3.5. Experimental validation

A desktop computer numerical control (CNC) machine tool (Taig Tools) is used for the experimental studies conducted in this paper. It is a three-axis machine tool operated by individual stepper motors. The resolution of each feed axis is 5.08 µm.

The microscope warm-up process often causes small displacements of the optical parts inside the microscope before they reach a thermal equilibrium. Therefore, a test was implemented to determine the microscope warm-up time. In this test, the authors took the measurement via the microscope at the same command tool center point (TCP) coordinates for one fiducial every five minutes after the microscope was turned on. The results, shown in Fig. 10, indicate the microscope reaches thermal equilibrium state after 80 min and, if the microscope is not sufficiently warmed up, there are roughly 10 µm, 25 µm, 20 µm errors in the X-, Y-, and Z-axis displacement measures, respectively.

To validate the proposed method, the machine tool is jogged to specific positions while the microscope is at thermal equilibrium, and a single fiducial is measured. In this study, the machine tool is jogged to 25.4 µm, 50.8 µm, 76.2 µm, 101.6 µm, and 127 µm in all three directions. Additionally, three dial indicators with resolutions of 1 µm are used to measure the machine tool displacements. Figure 11a shows the experimental set-up.

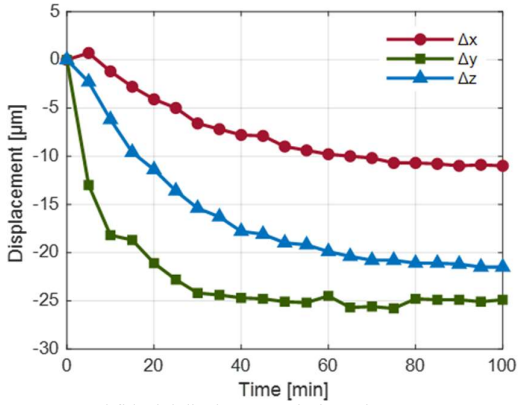

Fig. 10: Measured fiducial displacement during microscope warm up test.

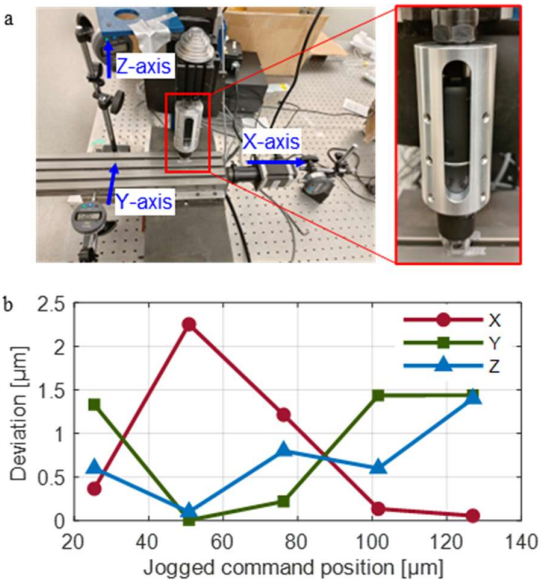

Fig. 11: (a) Experimental set up and (b) measured differences between dial indicator and microscope measurements.

Figure 11b shows the deviation between the dial indicator and microscope measurements in the X, Y, and Z-axis directions for all five jog motions. The results show that when the microscope is at thermal equilibrium the proposed measurement method can achieve a maximum measured deviation of < 2.3× the resolution of the dial indicator, which is less than one feed axis resolution.

4. Thermal error modeling and prediction

4.1. Experimental setup

Eight fiducials, denoted F1 … F8, are attached to the worktable, as shown in Fig. 12. To monitor temperature changes, two thermocouples, denoted TC1 and TC2, are mounted to the machine tool bed (one near the motor and one at the opposite end to determine potential temperature variation across the bed), one thermocouple, denoted TC3, is mounted to the machine tool column (Fig. 13), and one thermocouple, denoted TC4, is set far from the machine tool to monitor the room temperature. Even though four thermocouples cannot create a full map of the machine tool temperature distribution, the thermocouples monitor temperature variations at critical points (e.g., bed, spindle), indicating changes in the thermal state. For each machine tool thermal state, the eight fiducials are measured using the procedure in Section 3 in the order F1 to F8. All measurements are taken after the microscope has reached thermal equilibrium.

To examine machine tool repeatability, the eight fiducials were measured five times, denoted M0, M1, M2, M3, and M4, in a cold state. The temperature change during this experiment and the measurement durations are shown in Fig. 14. During this experiment, the temperature of the side of the bed without the X-axis motor (except for some outliers) and the column remained within 0.3 ℃, while the temperature on the side of the bed nearest to the motor and the room temperature increased and decreased, respectively, by approximately 0.8 ℃. The four measured displacements relative to the measurements for the M0 thermal state are shown in Fig. 15. The displacements are all less than one half of the machine tool resolution, indicating the machine tool repeatability will not significantly affect thermal error measurements.

4.2. Thermal error modeling and prediction

In this study, an error model [24] with nine error parameters is proposed as

$$\mathbf{E} = \left[\Delta E_X, \Delta E_Y, \Delta E_Z, \Delta E_A, \Delta E_B, \Delta E_C, \Delta E_{X0Y}, \Delta\alpha_X, \Delta\alpha_Y\right] \tag{21}$$

where the model parameters are illustrated in Fig. 16 and described in Table 1. Due to the Z-axis stroke limit of the machine tool in this study, all fiducials are located on the top surface of the worktable. Therefore, the Z-axis thermal expansion error and the squarenesses between the X and Z axes and the Y and Z axes are not included in the model. For the i^{th} fiducial, the relation between the error model parameters and the measured displacements $\left[\Delta x, \Delta y, \Delta z\right]_M^{(i)}$ is

$$\left[\Delta x, \Delta y, \Delta z\right]_M^{(i)} = \mathbf{S}^{(i)} \cdot \mathbf{E} \tag{22}$$

where $\mathbf{S}^{(i)}$ is the sensitivity matrix of the measured displacements to the error model parameters; that is

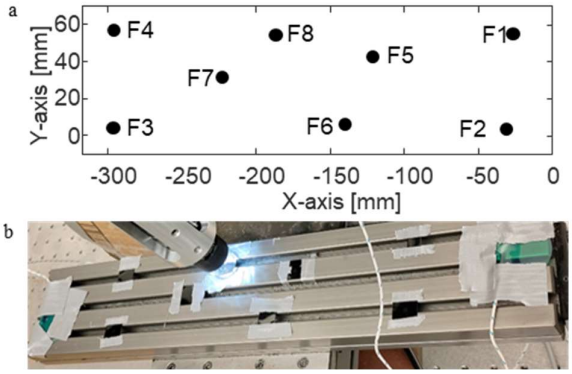

Fig. 12: (a) Locations of fiducials on worktable and (b) worktable photograph.

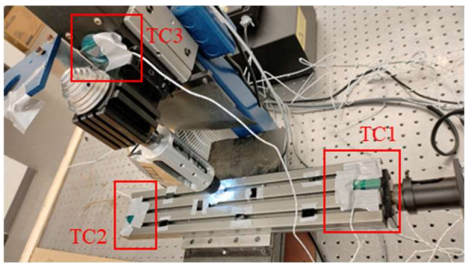

Fig. 13: Thermocouple locations on machine tool. TC4 is located far from machine tool to monitor room temperature.

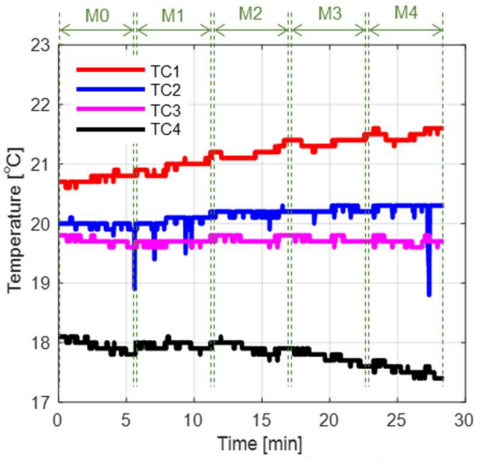

Fig. 14: Thermocouple measurement during experiment in cold state.

Table 1 Description of error model parameters defined in MCF.

Symbol	Description
ΔE_X	Positional error along X-axis
ΔE_Y	Positional error along Y-axis
ΔE_Z	Positional error along Z-axis
ΔE_A	Angular error about X-axis
ΔE_B	Angular error about Y-axis
ΔE_C	Angular error about Z-axis
ΔE_{X0Y}	Squareness between X- and Y- axes

$\Delta\alpha_X$	Linear thermal expansion along X-axis
$\Delta\alpha_Y$	Linear thermal expansion along Y-axis

$$\mathbf{S}^{(i)}=\begin{bmatrix}1 & & & -y_c^{(i)} & -y_c^{(i)} & x_c^{(i)} & \\ & 1 & & x_c^{(i)} & & & y_c^{(i)} \\ & & 1 & y_c^{(i)} & -x_c^{(i)} & & \end{bmatrix} \quad (23)$$

and $[x_c, y_c]^{(i)}$ in Eq. (23) is the command TCP coordinate in the MCF of the i^{th} fiducial.

The actual TCP is determined through D-H matrix [25]

$$\begin{bmatrix}x_a\\y_a\\z_a\\1\end{bmatrix}=\begin{bmatrix}1 & 0 & 0 & 0\\ \Delta E_{XOY} & 1 & 0 & 0\\ 0 & 0 & 1 & 0\\ 0 & 0 & 0 & 1\end{bmatrix}\begin{bmatrix}1 & -\Delta E_C & \Delta E_B & \Delta E_X\\ \Delta E_C & 1 & -\Delta E_A & \Delta E_Y\\ \Delta E_B & \Delta E_A & 1 & \Delta E_Z\\ 0 & 0 & 0 & 1\end{bmatrix}\begin{bmatrix}(1+\Delta\alpha_X) & 0 & 0 & 0\\ 0 & (1+\Delta\alpha_Y) & 0 & 0\\ 0 & 0 & 1 & 0\\ 0 & 0 & 0 & 1\end{bmatrix}\begin{bmatrix}x_c\\y_c\\z_c\\1\end{bmatrix} \quad (24)$$

where $[x_c, y_c, z_c]$ and $[x_a, y_a, z_a]$ are the command and actual TCP coordinates, respectively. The predicted thermal errors are

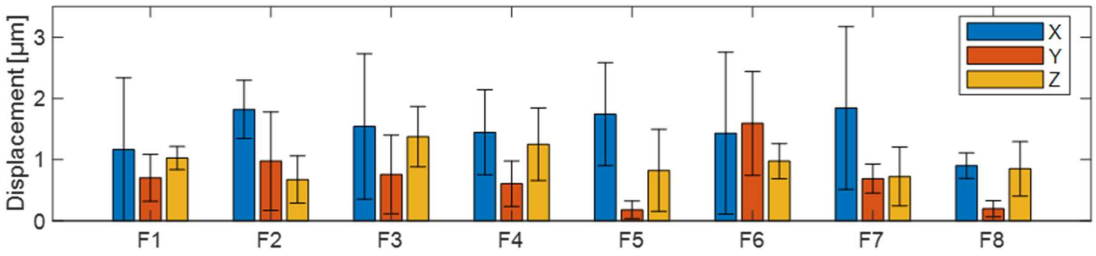

Fig. 15: Average fiducial displacements of measurements M1, M2, M3, and M4 relative to measurement M0 during experiment in cold state. Error bars indicate one standard deviation

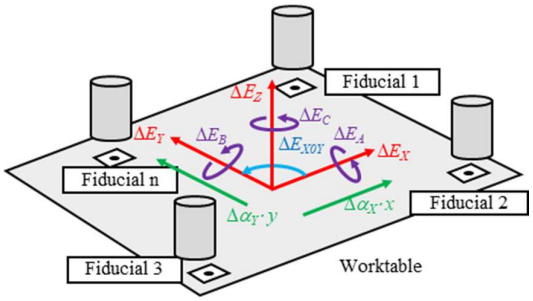

Fig. 16: Illustration of thermal error model parameters.

$$\left[e_x, e_y, e_z\right]=\left[x_a, y_a, z_a\right]-\left[x_c, y_c, z_c\right] \quad (25)$$

Based on Eqs. (21)-(23), three linear equations are obtained from each fiducial. The error parameters are calculated using the least-squares method as

$$\mathbf{E}=\begin{bmatrix}\mathbf{S}^{(1)}\\ \vdots \\ \mathbf{S}^{(n)}\end{bmatrix}\backslash\begin{bmatrix}[\Delta x, \Delta y, \Delta z]_M^{(1)T}\\ \vdots \\ [\Delta x, \Delta y, \Delta z]_M^{(n)T}\end{bmatrix}, n\geq 3 \quad (26)$$

where T donates a matrix transpose, and n represents the number of fiducials measured to construct the model.

4.3. Experimental study

In the second experiment a heat source is directed towards the machine tool column to create a distinct change in the machine tool thermal state. The thermocouple temperature profiles are shown in Fig. 17. The eight fiducials are measured at the beginning of the test, denoted Mh0, the heat source is disengaged at approximately 55 min, and the eight fiducials are measured every 30 min for 2.5 hr. These six measurements are denoted Mh1, Mh2, Mh3, Mh4, Mh5, and Mh6. At each of these six measurements two thermal error models are constructed: one using fiducial set 1 consisting of fiducials F1, F2, F3, and F4, which are located at four corners of the table, and one using fiducial set 2 consisting of fiducials F2, F4, F5, and F7, which are roughly diagonal along the table. These fiducial sets are selected as they spatially span the axes.

Figures 18 and 19 show the errors between the predicted and measured displacements from machine tool thermal states Mh1 to Mh0 for thermal error models constructing using fiducial sets 1 and 2, respectively. Figures 20 and 21 show the average absolute errors between the predicted and measured displacements from the last six machine tool thermal states (i.e., Mh1-Mh6) to machine tool thermal state Mh0 for every fiducial in all three machine tool directions for thermal error models constructed using fiducial sets 1 and 2, respectively.

The data in Figures 18 and 19 indicate a systematic error in Fiducial 6 for the X and Y measurements, where the positive error denotes thermal deformation in the positive direction. In Figs. 18 and 19 Fiducial 6 error is given as a numerical value and not included as part of the color map. The reason for this error is currently under investigation. These results show there is no spatial correlation to the errors between the predicted and measured thermally induced displacements. The results in Figs. 20 and 21 show that for both sets of fiducials, the models constructed at each measurement, on average, predict the error within one machine tool resolution, except for Fiducial 4 in Figure 21 which was within two machine tool resolutions, for the fiducials used to construct the models and within four

machine tool resolutions for the validation fiducials, i.e., those fiducials not used to construct the models. The models using fiducial set 1 yield less error than the models using fiducial set 2 for the fiducials used to construct the models; however, the performance was similar when considering the fiducials not used to construct the models. Further research is needed to understand the best location to place the fiducials and how many fiducials are needed to construct accurate thermal error models.

Figures 22 and 23 show the predicted thermal error heat maps for thermal error models from machine tool thermal states Mh1 to Mh0 constructed using fiducial sets 1 and 2, respectively. The magnitudes for both models are similar; however, the Z-axis errors are twice as large for the model using fiducial set 2 compared to the model using the fiducial set 1. The results show a strong spatial dependence to the predicted error for both models. For the X- and Z-axes, the predicted errors increase in the negative and positive X directions, respectively. However, the direction of increasing Y-axis predicted error is opposite for the two models. This can be explained by interrogating the model parameters, which are given in Table 2. The models have similar positional error coefficients, i.e., ΔE_X, ΔE_Y, and ΔE_Z, coefficients of linear thermal expansion along the X-axis, (i.e., $\Delta\alpha_X$), and squareness coefficients (i.e., ΔE_{XoY}); however, the coefficients of angular changes about the X and Z axes, i.e., ΔE_A and ΔE_C, respectively, and the coefficient of linear thermal expansion along the Y-axis, i.e., $\Delta\alpha_Y$, are very different in magnitude and have the opposite signs. A comparison of Figures 20 and 21 demonstrates the model constructed with fiducial set 1 provides better error prediction than the model constructed with fiducial set 2.

5. Summary and Conclusions

In this study, a novel method is proposed to measure the thermal errors of a three-axis machine tool. A wireless microscope is adopted for the measurement of unique, custom-designed fiducials mounted to the worktable, and the displacement due to the machine tool thermal deformation is determined through an image processing algorithm. For each fiducial, three images are taken at each thermal state to determine the displacements in the machine tool X- and Y-axis directions, and five images are taken at each thermal state to estimate the Z-axis displacement. The measurement method is experimentally validated through measuring the displacement of one fiducial as it is jogged to various locations. In addition, a least-squares-based thermal error model is proposed in which the error parameters are determined from the measurement of multiple fiducials attached on the worktable to predict the machine tool thermal error within the machine tool work volume.

The conclusions of this study are as follows:

- The displacements in machine tool X- and Y-axes can be accurately determined by the deviation of the COR position located at the FCF.
- The displacements in the machine tool Z-axis direction can be determined through the comparison between the contrast curves of the two thermal states, obtained from five images with different Z-positions for each thermal state.
- The error parameters determined through the fiducials located at the corners of the machine tool workspace predict the thermal errors more accurately than the error parameters determined by fiducials located roughly diagonally across the worktable.
- The unique row-and-column numbering system for the ellipse pattern allows for the measurement of planar thermal errors that are of any size, which is advantageous for machine tools that experience large thermal errors.

In the future, a thermal error compensation strategy is planned based on the measurement and modeling method. To achieve real-time thermal error compensation, the image-processing algorithm will be updated to be faster for near real-time calculations. In addition, a high-order thermal error is needed to achieve a higher thermal error prediction accuracy across the work volume. It can be expected that the proposed method will be fast, accurate, cheap, and practical for thermal error measurement and compensation in production facilities.

Acknowledgement

The authors would like to express appreciation for the support from the following financial assistance award: 70NANB22H180 from the U.S. Department of Commerce, National Institute of Standards and Technology.

†Disclaimer

Certain commercial equipment, instruments, or materials are identified in this paper in order to specify the experimental procedure adequately. Such identification is not intended to imply recommendation or endorsement by the National Institute of Standards and Technology, nor is it intended to imply that the materials or equipment identified are necessarily the best available for the purpose. This material is declared a work of the U.S. Government and is not subject to copyright protection in the United States. Approved for public release; distribution is unlimited.

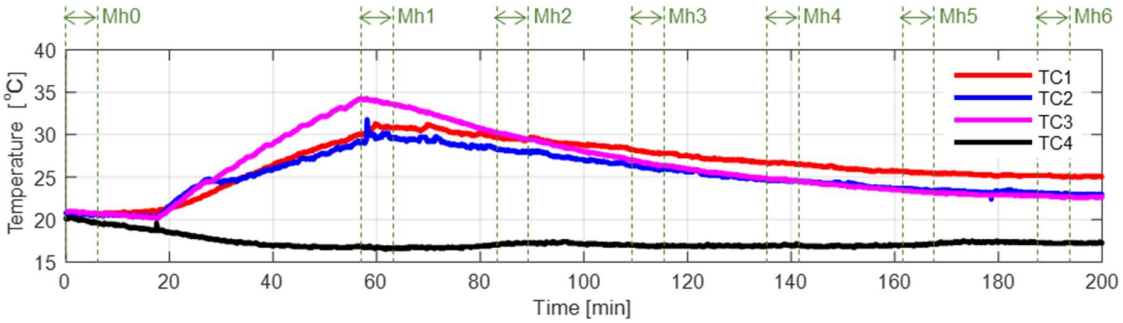

Fig. 17: Thermocouple measurements during experiment with external heat source.

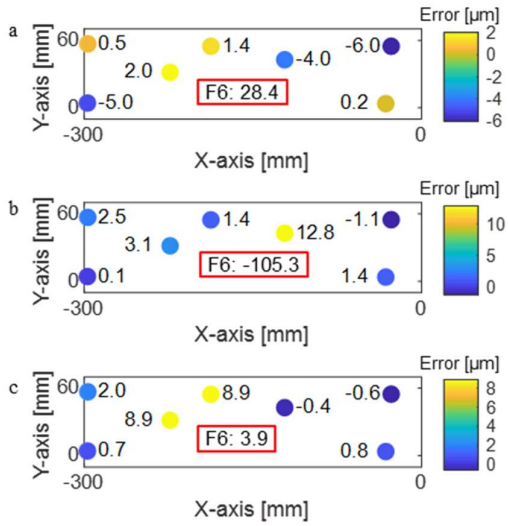

Fig. 18: (a) X axis, (b) Y axis, and (c) Z axis errors between predicted and measured displacements from machine tool thermal state Mh1 to machine tool thermal state Mh0 using thermal error model constructed with fiducial set 1. Red boxes indicate F6 errors.

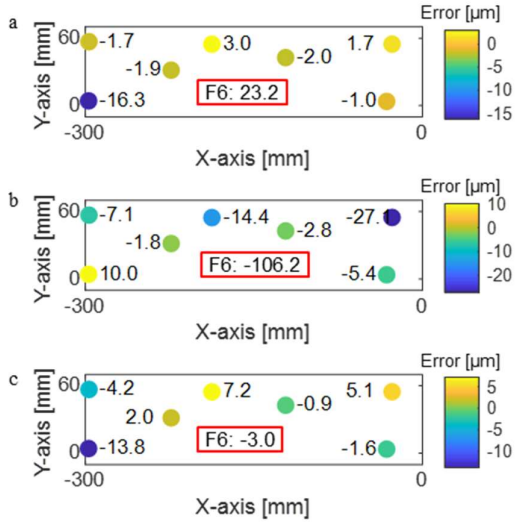

Fig. 19: (a) X axis, (b) Y axis, and c) Z axis errors between predicted and measured displacements from machine tool thermal state Mh1 to machine tool thermal state Mh0 using thermal error model constructed with fiducial set 2. Red boxes indicate F6 errors.

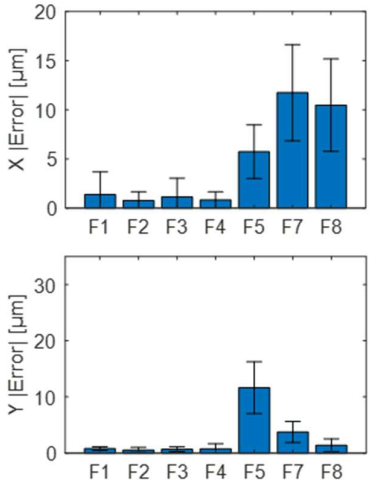

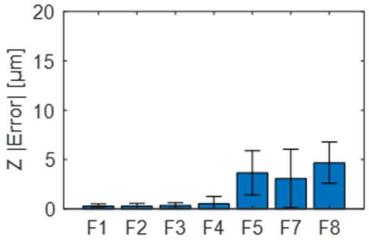

Fig. 20: Average absolute errors between predicted and measured displacements for X (top), Y (middle), and Z (bottom) axes and all eight fiducials using models constructed from fiducial set 1. Error bars indicate one standard deviation. Results for fiducial 6 are not shown.

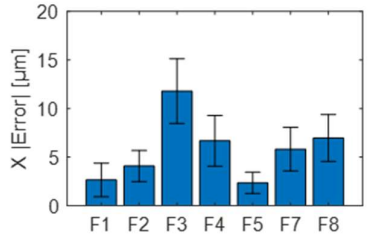

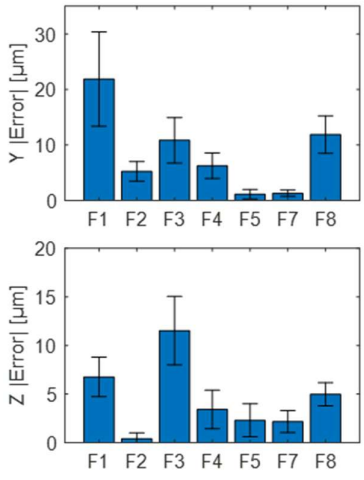

Fig. 21: Average absolute errors between predicted and measured displacements for X (top), Y (middle), and Z (bottom) axes and all eight fiducials using models constructed from fiducial set 2. Error bars indicate one standard deviation. Results for fiducial 6 are not shown.

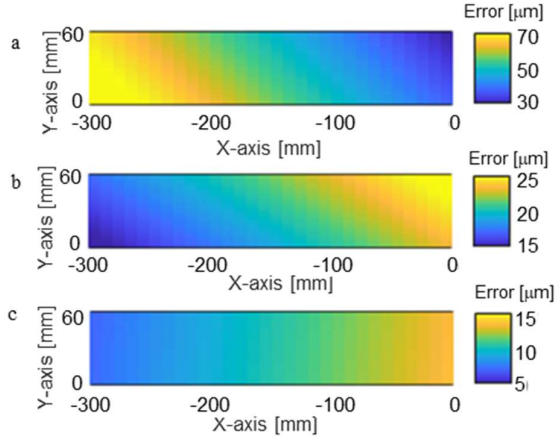

Fig. 22: Heat map of predicted errors on worktable for model constructed at measurement Mh1 using fiducial set 1: (a) X error, (b) Y error, and (c) Z error.

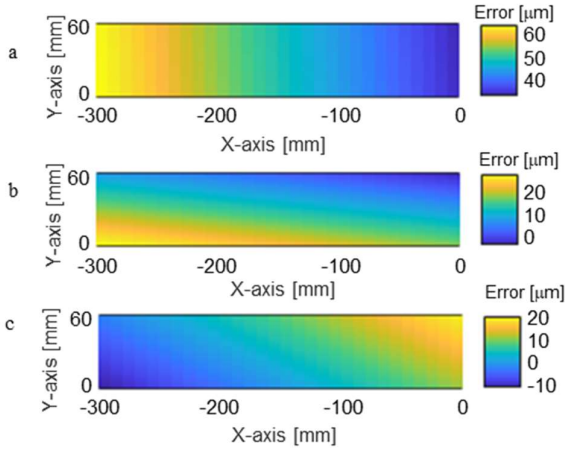

Fig. 23: Heat map of predicted errors on worktable bed for model constructed at measurement Mh1 using fiducial set 2: (a) X error, (b) Y error, and (c) Z error.

Table 2 Thermal error model parameters for models constructed at measurement Mh1 for both fiducial sets.

Symbol	Unit	Set 1	Set 2
ΔE_X	[µm]	39.4	36.6
ΔE_Y	[µm]	23.4	19.6
ΔE_Z	[µm]	13.0	11.4
ΔE_A	[mrad]	-0.052	3.927
ΔE_B	[mrad]	-0.646	-1.484
ΔE_C	[mrad]	0.593	-6.632
ΔE_{X0Y}	[mrad]	1.658	0.873
$\Delta \alpha_X$	[µm/mm]	-0.125	-0.102
$\Delta \alpha_Y$	[µm/mm]	0.046	-0.325

References

[1] Schmitz TL, Ziegert JC, Canning JS, Zapaata R. Case study: comparison of error sources in high-speed milling. Prec Eng 2008;32,2:126-133.
[2] Andolfatto L, Lavernhe S, Mayer JRR. Evaluation of servo, geometric and dynamic error sources on five-axis high-speed machine tool. Int J Mach Tool Manuf 2011;51:787-796.
[3] Mayr J, Jedrzejewski J, Uhlmann E, Donmez MA, Knapp W, Hartig F, Wendt K, Moriwaki T, Shore P, Schmitt R, Brecher C, Wurz T, Wengener K. Thermal issues in machine tool. CIRP Ann 2012;61,2:771-791.
[4] Bryan J. International states of thermal error research (1990). CIRP Ann 1990;39,2:945-956.
[5] Neugebauer R, Drossel WG, Ihlenfeldt S, Richter C. Thermal interactions between the process and workpiece. Procedia CIRP 2012;4:63-66.
[6] Anandan KP, Ozdoganlar OB. Aanlysis of error motions of ultra-high-speed (UHS) micromachining spindles. Int J Mach Tool Manuf 2013;70:1-14.
[7] Donmez MA, Hahn MH, Soons JA. A novel cooling system to reduce thermal-inuced errors of machine tools. CIRP Ann 2007;56,1:521-524.
[8] Ramesh R, Mannan MA, Poo AN, Error compensation in machine tools – a review Part II: thermal errors. Int J Mach Tool Manuf 2000;40,9:1257-1284.
[9] Liang RJ, Ye WH, Zhang HYH, Yang QF, The thermal error optimization models for CNC machine tools, Int J Adv Manuf Technol 2012;63,9:1167-1176.
[10] Li Y, Zhao WH, Lan SH, Ni J, Wu WW, Lu BH, A review on spindle thermal error compensation in machine tools, Int J Mach Tool Manuf 2015;95:20-38.
[11] Cui G, Lu Y, Gao D, Yao Y, A novel error compensation implementing strategy and realizing on Simens 840 D CNC systems, Int J Adv Manuf Technol 2012;61:595-608.
[12] Gebhardt M, Mayr J, Furrer N, Widmer T, Weikert S, Knapp W, High precision grey-box model for compesnation of thermal errors on five-axis machines, CIRP Ann 2014;63:509-512.
[13] Zimmermann N, Lang S, Blaser P, Mayr J, Adaptive input selection for thermal error compensation models, CIRP Ann, 2020;69:485-488.
[14] Biermann D, Holtermann R, Menzel A, Schumann S. Modelling and simulation of thermal errects in internal traverse grinding of hardened bearing steel. CIRP Ann 2016;65,1:321-324.
[15] Li Y, Yu M, Bai Y, Hou Z, Wu W. A review of thermal error modeling method for machine tools. Appl Sci 2021;11,5216.
[16] Gao Q, Zhang P. There error recognition and compensation for the numerical control machine tools based on laser testing technology. Open Phys J 2019;17,1:857-862.
[17] Ashok SD, Samuel GL. Modeling, measurement, and evaluation of spindle ratial errors in a miniaturized machine tool. Int J Adv Manuf Technol 2012;59,5:455-461.
[18] Ibaraki S, Okunura R. A machining test to evaluate thermal influence on the kinematics of a five-axis machine tool. Int J Mach Tool Manuf 2021;163:103702.
[19] ISO 230-1, Test code for machine tools – Part 1: geometric accuracy of machines operating under no-load or quasi-state conditions, 2012
[20] Ibaraki S, Blaser P, Shimoike M, Takayama N, Nakaminami M, Ido Y. Measurement of thermal influence on a two-dimensional motion trajectory using a tracking interferometer. CIRP Ann 2016;65,1:483-486.

[21] Mori M, Irino N, Shimoike M, A new measurement method for machine tool thermal deformation on a two-dimensional tracking interferometer. CIRP Ann 2019;86,1:551-554.
[22] Brecher C, Spierling R, Fey M, Neus S. Direct measurement of therml-elastic errors of a machine tool. CIRP Ann 2021;70,1-333-336.
[23] Pertuz S, Puig D, Garcia MA. Analysis of focus measure operators for shape-from-focus. Pattern Recognit 2013;46,5:1415-1432.
[24] Vogl GW, Rexford A, Li Z, Landers RG, Kinzel EC, Donmez MA, Chalfoun J. Vision-based thermal drift monitoring method for machine tools. CIRP Ann 2023;72,1:301-304.
[25] Li Z, Sato R, Shirase K, Samamoto S. Study on the influence of geometric errors in rotary axes on cubic-machining test considering the workpiece coordinate system. Prec Eng 2021;71:36-46.